

# The interfacial embedding of halogen-terminated carbon dots produces highly efficient and stable flexible perovskite solar cells

Chen Liu<sup>1</sup>, Ning Jia<sup>1</sup>, Ji-zhou Zhai<sup>2</sup>, Peng-zhen Zhao<sup>1</sup>, Peng-fei Guo<sup>1,3,\*</sup>, Hong-qiang Wang<sup>1,3</sup>

<sup>1</sup>State Key Laboratory of Solidification Processing, Center for Nano Energy Materials, School of Materials Science and Engineering, Northwestern Polytechnical University and Shaanxi Joint Laboratory of Graphene (NPU), Xi'an 710072, China;

<sup>2</sup>Xi'an Institute for Innovative Earth Environment Research, Xi'an 710061, China;

<sup>3</sup>Chongqing Innovation Center, Northwestern Polytechnical University, Chongqing 401135, China

**Abstract:** Organic-inorganic hybrid perovskite films made by low-temperature solution processing offer promising opportunities to fabricate flexible solar cells while formidable challenges regarding their environmental and mechanical stability remain due to their ionic and fragile nature. This work explores the possibility of chemical crosslinking between adjacent grains by the interfacial embedding of laser-derived carbon dots with halogen-terminated surfaces to improve the flexibility and stability of the polycrystalline films. A series of halogen-terminated carbon dots was generated in halobenzene solvents by pulsed laser irradiation in the liquid, and were then placed in the surface and grain boundaries of the perovskite film by an antisolvent procedure, where an immiscible solvent was poured onto the coating surface with a suspension containing carbon dots and perovskite precursors to cause precipitation. Strong interaction between perovskite and the carbon dots results in effective defect passivation, lattice anchoring and a change in the carrier dynamics of the perovskite films. Because of this, unencapsulated flexible perovskite solar cells after the interfacial embedding have power conversion efficiencies up to 20.26%, maintain over 90% of this initial value for 90 days under a relative humidity of 40% and have a thermal stability of 200 h even at 85 °C. The flexible devices withstand mechanical deformation, retaining over 80% of their initial values after 500 bend cycles to a radius of curvature of 4 mm.

**Key Words:** Interfacial embedding; Pulsed laser irradiation; Stability; Halogen-terminated carbon dots; Flexible perovskite solar cells

## 1 Introduction

Organic-inorganic hybrid perovskite materials have drawn tremendous research attention in photovoltaic field, owing to their excellent optoelectronic and unique physical properties such as tunable bandgap<sup>[1]</sup>, strong absorption coefficient<sup>[2]</sup>, and long carrier diffusion length<sup>[3]</sup>. Benefiting from these merits, the recorded power conversion efficiency (PCE) of perovskite-based solar cells (PSCs) has risen from 3.8% to 25.7% in a decade<sup>[4]</sup>. Moreover, one attractive advantage of PSCs over the conventional silicon-based solar cells is the capability of low-temperature solution-processing, which enables the device fabrication on various flexible substrates<sup>[5]</sup>. The remarkable effort devoted to optimizing flexible PSCs in terms of the device architecture<sup>[6]</sup>, flexible substrate<sup>[7]</sup> and charge collecting electrode<sup>[8]</sup> has demonstrated a positive effect on boosting the PCE, while the long-term stability against external stimuli such as moisture<sup>[9]</sup>, thermal stress<sup>[10]</sup> and mechanical deformation<sup>[11]</sup>, remains as the key problem restricting the commercialization progress of flexible PSCs. One of the main reasons behind the obstacles is

associated with the ionic and fragile nature of solution-processed perovskites<sup>[9,12]</sup>. Abundant defects are formed at the surfaces and grain boundaries (GBs) of polycrystalline perovskite films<sup>[13-15]</sup>, which could serve as the invasion sites of film degradation as well as the initial sites of film fracture, and contribute consequently to inferior environmental and mechanical stability of flexible PSCs.

Surface and GB engineering of perovskite films is thus of paramount importance and particularly urgent not only for inhibiting the degradation of the perovskite active layer, but synchronously promoting superior robustness against mechanical deformation of flexible PSCs<sup>[5,9,13-15]</sup>. Universal proposal that employs molecule or polymer additives as an interfacial mediator to stabilize and crosslink the polycrystalline perovskite films based on Lewis acid-base interaction or ionic-bonding, has made steady progress in inhibiting macroscopic cracks of the film and even microscopic distortion of the perovskite lattice<sup>[5,9]</sup>. A notable example is that patching adjacent perovskite grains through incorporating a photo-crosslinked fullerene network into the perovskite films not only significantly improves the

Received date: 27 Jun. 2022; Revised date: 12 Aug. 2022

\*Corresponding author. E-mail: [guopengfei@nwpu.edu.cn](mailto:guopengfei@nwpu.edu.cn)

Copyright©2022, Institute of Coal Chemistry, Chinese Academy of Sciences. Published by Elsevier Limited. All rights reserved.

DOI: 10.1016/S1872-5805(22)60639-5

mechanical stability but also exhibits an outstanding PCE of 18.1% for flexible PSCs<sup>[9]</sup>. However, it cannot be ignored that most of these additives more or less block the charge transport at the GBs of perovskite films or the interface in PSCs due to the intrinsic insulativity, leading generally to less-than-ideal PCEs by sacrificing photocurrent density.

This highlights the need to explore new additives that could be introduced at GBs and would synchronously improve the environmental and mechanical stability of flexible PSCs without the trade-off of photovoltaic performance. As respected, 0D nanocrystals with sizes below 10 nm exhibit novel properties compared to their bulk counterparts and molecular additives<sup>[16]</sup>. In particular, carbon dots (CDs) are an emerging class of carbon-dominated nanomaterials, which have attracted considerable attention for photovoltaics applications, owing to the tunability in physical/chemical properties and the compatibility with other materials<sup>[17]</sup>. Inspired by the success of the widely adopted nanocrystal additives in rigid PSCs<sup>[18-20]</sup>, we thus note that incorporating CDs into perovskite films is anticipated to provide more spaces to advance the development of highly efficient, stable and robust flexible PSCs (FPSCs), which however has been rarely reported. The main reason could be attributed to the technological hurdles of generating well-defined CDs with tailored surface states in the desired solvents as well as subsequent interfacial embedding of them in the perovskite active layer.

Herein, we developed an effectively chemical crosslinking strategy through interfacial embedding of well-defined nanoparticles to improve the flexibility and carrier dynamics of perovskite films. A series of halogen-terminated CDs (CDs-T, T=F, Cl, Br) were directly generated in halobenzenes via the technology of pulsed laser irradiation in liquid (Scheme 1a), which were then in site introduced into the perovskite film by employing the resultant colloidal solution as antisolvents (Scheme 1b), and

consequently configuring a planar *n-i-p* flexible PSC. The laser-derived CDs-T with high crystallinity and functionality were located both at the surface and GBs of the perovskite film (Scheme 1c). Highly stable and flexible perovskite films were thus constructed through strong chemical interactions between CDs-T and perovskite, and allowed us to fabricate flexible PSCs with a PCE up to 20.26%. More importantly, unencapsulated PSCs retained over 90% of their initial PCE after 90 days under a relative humidity of 40% as well as delivering a thermal stability of 200 h under thermal stress of 85 °C. Also, the CDs-T embedded flexible PSCs demonstrated superior robustness against mechanical deformation, i.e., retaining over 80% of their initial value after 500 bending cycles at a curvature radius of 4 mm.

## 2 Experimental

### 2.1 Materials

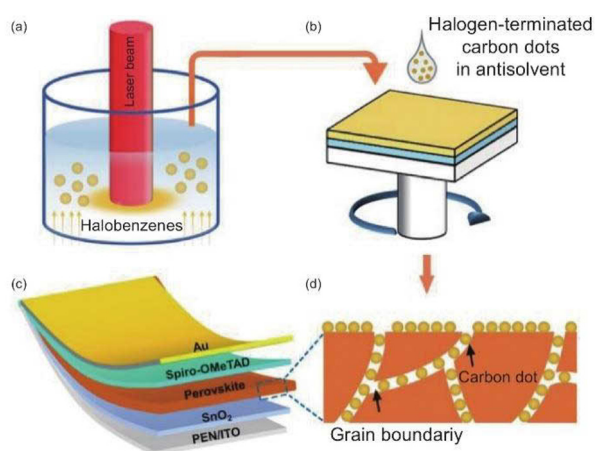
Unless stated otherwise, all materials were purchased from Sigma-Aldrich and used as received. The flexible PEN/ITO substrates were obtained from Peccell and etched by a commercial corporation. The SnO<sub>2</sub> colloidal dispersion (tin (IV) oxide, 15% in H<sub>2</sub>O colloidal dispersion) was purchased from Alfa Aesar. Spiro-OMeTAD(2,2',7,7'-Tetrakis [N,N-di(4-methoxyphenyl)amino]-9, 9'-spirobifluorene, ≥99.8% purity), 4-tert-butylpyridine (tBP, ≥99.9% purity) and lithium-bis (trifluoromethanesulfonyl) imide (Li-TFSI, ≥99.9% purity) were supplied by Xi'an Polymer Light Technology Corp.

### 2.2 Preparation of halogen-terminated carbon dots

To terminate the surfaces of CDs with halogen, a series of halobenzenes (fluobenzene, chlorobenzene and bromobenzene) were selected as both the carbon and the halogen sources. These solvents were put into a reaction cell under an inert environment and subjected to irradiation by a non-focused pulsed laser beam (repetition rate: 10 Hz, pulse width: 8 ns, beam diameter: 8 mm), during which, ultrasonication was employed to ensure homogeneous reactions in corresponding solvents. The optimized processing parameters are a laser wavelength of 355 nm, a fluence of 200 mJ/pulse cm<sup>-2</sup> and a radiation time of 20 min, following our previous work<sup>[18]</sup>.

### 2.3 Device fabrication

The flexible PEN/ITO substrates were cleaned with successive sonication in detergent, deionized water, acetone and ethanol for 20 min, and then dried under N<sub>2</sub> flow and treated by ozone plasma for 10 min to remove the organic residual and enhance the wettability. For the preparation of the electron transport layer, the as-purchased SnO<sub>2</sub> colloidal solution was diluted by water (1:3%), and then spin-coated onto the clean PEN/ITO substrates at 4000 r min<sup>-1</sup> for 20 s, followed by the annealing at 130 °C for 30 min. For the preparation of perovskite films, a 1.55 mol L<sup>-1</sup> perovskite precursor solution containing CsI (20.13 mg), FAI (226.57 mg), PbI<sub>2</sub> (750.31 mg), MABr (17.36 mg) and MACl (20.93



Scheme 1 Schematic illustration of preparation of CDs-T via the technology of pulse laser irradiation in liquid and subsequent interfacial embedding of CDs-T in the perovskite active layer and its flexible PSC.

mg), was stirred in a mixture (1 mL) of DMF and DMSO (4 : 1 v/v) at 60 °C for 2 h. The resulting solutions were coated onto the PEN/ITO/SnO<sub>2</sub> substrate by a consecutive two-step spin-coating process at 1 000 and 4 000 r min<sup>-1</sup> for 10 and 30 s, respectively. During the second step, 200 uL antisolvent or its colloid solution was immediately poured on the spinning substrate 10 s prior to the end of the program. Thereafter, the substrate was put onto a hotplate for 30 min at 100 °C, forming the perovskite films with a composition of Cs<sub>0.05</sub>FA<sub>0.81</sub>MA<sub>0.14</sub>PbI<sub>2.55</sub>Br<sub>0.45</sub>. After the deposition of perovskite films, a precursor solution of a hole transport layer (HTL) material, where the (spiro-OMeTAD)/chlorobenzene solution (72.3 mg mL<sup>-1</sup>) with the addition of 28.8 uL tBP and 17.5 μL Li-TFSI/acetonitrile (520 mg mL<sup>-1</sup>), was then deposited by spin coating at 5 000 r min<sup>-1</sup> for 30 s. Finally, an 80 nm thick Au electrode was deposited by thermal evaporation. The active area of this electrode was 0.1 cm<sup>2</sup>, which was calculated by a mask plate and further determined by an optical microscope.

## 2.4 Characterization and measurements

Transmission electron microscopy (TEM, FEI Talos F200X) was performed to determine the size and structure of halogen-terminated CDs. Raman spectroscopy (Renishaw) and X-ray photoelectron spectroscopy (XPS, Axis Supra) were then employed to analyze the graphitization degree and surface composition of the laser-derived CDs. Cyclic voltammetry measurements were carried out on a CHI voltammetry analyzer for determining the highest occupied molecular orbital (HOMO) and the lowest unoccupied molecular orbital (LUMO) levels of the CDs at room temperature under the protection of dry nitrogen<sup>[18,21,22]</sup>. Tetrabutylammonium hexafluorophosphate (n-Bu<sub>4</sub>NPF<sub>6</sub>, 0.1 mol L<sup>-1</sup>) was used as the supporting electrolyte. The conventional three-electrode configuration consists of a platinum disk working electrode, a platinum wire counter electrode, and an Ag/AgCl reference electrode. LUMO energy level was calculated by  $-e(-E_{\text{on}}^{\text{red}} + 4.80)$  (eV). Cyclic voltammograms were obtained at a scan rate of 100 mV s<sup>-1</sup>. For the perovskite films, the morphology was characterized by field emission scanning electron microscopy (SEM, FEI Verios G4). X-ray diffraction (XRD) patterns were recorded on a ANALYTICALX'pert PRO equipped with a diffracted beam monochromator, and a conventional cobalt target X-ray tube set to 40 kV and 30 mA. The binding energies and electronic structures of the perovskite films were further investigated by XPS and ultraviolet photoelectron spectroscopy (UPS). The Valance band (VB) spectra were measured with a monochromatic He I light source (21.22 eV) and a VG Scienta R4000 analyzer. The absorption was measured using an ultraviolet-visible (UV-vis) spectrophotometer (Perkin-Elmer Lambda 35). The steady-state photoluminescence (PL) spectra were measured using pulse laser as an optical excitation source (wavelength: 470 nm, Horiba FluorologFL-3), and time-resolved photoluminescence (TRPL) experiments were simultaneously performed by exciting at 470 nm.

Nanoindenter (Hysitron TI980) was employed to evaluate the mechanical performance of perovskite films.

For the characterization of flexible devices, simulated AM 1.5G irradiation (100 mW cm<sup>-2</sup>) was produced by a xenon-lamp-based solar simulator (Enlitech, Taiwan, China) for density-voltage (*J-V*) measurements of FPSCs. The light intensity was calibrated by a silicon (Si) diode (Hamamatsu S1133) equipped with a Schott visible-color glass filter (KG5 color-filter). A Keithley 2420 Source-Meter was used for *J-V* measurement with a scanning rate of 0.1 V s<sup>-1</sup>. The dark current-voltage (*I-V*) characteristics of the electron-only and hole-only devices were measured to calculate the defect density of perovskite films<sup>[3]</sup>. External quantum efficiencies (EQEs) were measured by an EQE measurement system (Enlitech, Taiwan). For the steady-state output measurement, the solar cells were put under the simulated AM 1.5G, 1-sun illumination to record the photocurrent under a bias voltage. Moisture-stability measurements of the non-encapsulated FPSCs were performed in a constant temperature & humidity incubator in dark. Thermal stability of the FPSCs was tested on a hot plate (85 °C) in a nitrogen atmosphere. PCEs of the devices were periodically measured in ambient air. For the mechanical stability, the FPSCs were tested for the bending measurements under either different curvature radii or cycles.

## 3 Results and discussion

As shown in Fig. 1a, it could be clearly observed that a certain amount of halobenzenes change from colorless to light yellow after laser irradiation (355 nm, 200 mJ/pulse cm<sup>-2</sup>). The typical Tyndall scattering shown in the right of Fig. 1a demonstrates the colloidal formation in halobenzenes. The colloidal solutions exhibit an excitation wavelength dependent photoluminescence (Fig. 1b), indicating the probable formation of CDs in halobenzenes<sup>[18]</sup>. To further determine these halobenzenes-derived nanoparticles, TEM and high resolution TEM (HRTEM) were employed to determine the size and crystal structure of the colloidal particles (Fig. 1c-e). All the colloidal solutions exhibit the monodispersity with an average size of about 2 nm by counting over 50 units (Fig. 1c-e). Lattice fringes with an inner-plane spacing at 0.213 nm corresponding to the (100) lattice fringe of ideal graphite<sup>[23]</sup>, are depicted in insets in Fig. 1c-e, confirming the generation of CDs by laser irradiation of halobenzenes. These results also indicate that the halogen is not likely to entry into the hexagonal lattice of CDs, and is more likely to be located at surface or between their interlayers. Raman spectra shown in Fig. 1f exhibit 2 typical peaks centered at 1 366 and 1 588 cm<sup>-1</sup> that is attributed to the *D* and *G* bands of the laser generated CDs, respectively. The intensity ratio of the *D*-band to *G*-band (*I<sub>D</sub>/I<sub>G</sub>*) is about 0.65, indicating the good crystalline nature of the CDs<sup>[24,25]</sup>.

XPS was employed to further verify the surface composition, especially the halogen-terminations of the CDs. It can be seen that the existence of F, Cl and Br in the laser

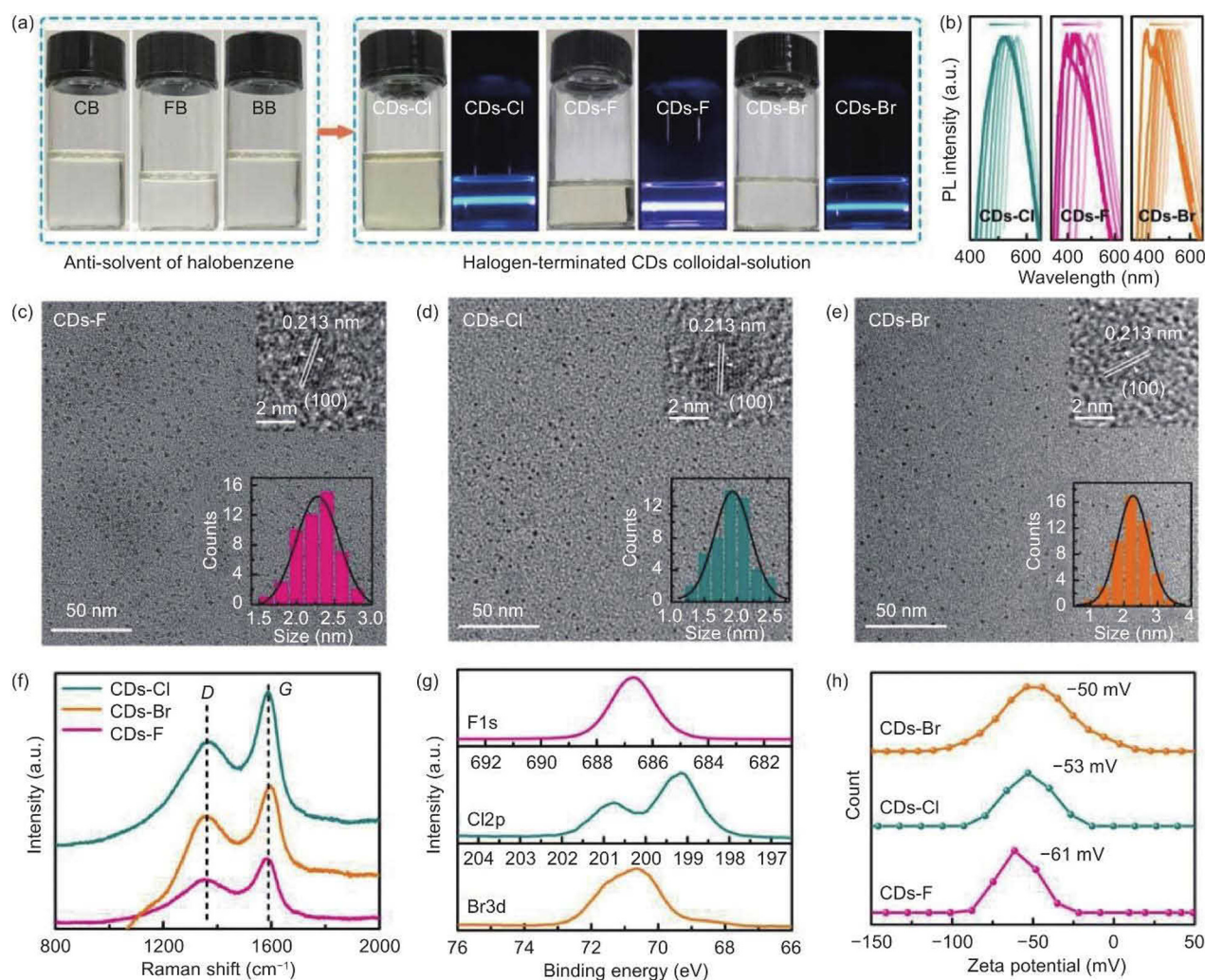


Fig. 1 (a) Laser generated CDs-T colloidal solutions with a typical Tyndall phenomenon in (CB) chlorobenzene, fluobenzene (FB) and bromobenzene (BB). (b) Normalized PL spectra of CDs-T colloidal solutions under excitation from 340 to 500 nm, in 20 nm increments. (c-e) TEM images of the CDs-T and their HRTEM images and size distributions (inset). (f) Raman spectra of solid CDs-T. (g) XPS spectra of F1s, Cl2p and Br3d. (h) ζ-potential spectra of CDs-T.

generated CDs is confirmed by the peaks of the binding energy in F1s, Cl2p and Br3d, respectively (Fig. 1g). Also, the ζ-potential measurements on all the colloidal solutions of CDs give a negative value reaching over  $-50$  mV (Fig. 1h), which suggests the terminated negative moieties of  $F^-$ ,  $Cl^-$ ,  $Br^-$  on the surface of resultant CDs<sup>[26]</sup>. In short, the surface of CDs could be directly terminated with halogens via the pulsed laser irradiation of halobenzenes, which is fundamentally different from those synthesized by conventional wet-chemical methods.

Following a typical antisolvent procedure, the tri-cation and dual-anion mixed perovskite films ( $CS_{0.05}FA_{0.81}MA_{0.14}PbI_{2.55}Br_{0.45}$ ) were fabricated on PEN/ITO/SnO<sub>2</sub> substrates by employing the colloidal solutions of halogen-terminated CDs as the antisolvent<sup>[18-20]</sup>. The FPSC devices with *n-i-p* planar configuration of PEN/ITO/SnO<sub>2</sub>/CsFAMA/spiro-OMeTAD/Au could be thus fabricated after the deposition of Spiro-OMeTAD HTL and Au electrode (see Experimental Section and Scheme 1d). We denote the reference perovskite as 'CsFAMA' and the CDs-embedded

perovskite as 'CsFAMA-T ( $T=F, Cl$  or  $Br$ )'. Fig. 2a shows the statistics of 50 devices with different amounts of CD embedding. The average PCEs rise from pristine 8.72% to 11.35% for CsFAMA-F devices, from 17.83% to 19.87% for CsFAMA-Cl devices, and from 12.14% to 13.72% for CsFAMA-Br devices, indicating the universal capacity of halogen-terminated CDs in boosting the PCE of FPSCs. Notably, the devices based on CsFAMA-Cl films deliver the best efficiency compared to those from CsFAMA-F and CsFAMA-Br, due to the advantages of chlorobenzene in growth of perovskite film during spin-coating process<sup>[27]</sup>. It should be noted that the comparison here is only for demonstration the pronounced capability of updating antisolvents of halobenzene to halogen-terminated CDs for boosting photovoltaic performance of FPSCs.

The antisolvent of chlorobenzene and its laser-derived colloidal solution of CDs-Cl were thus employed to exemplify the photovoltaic performance of FPSCs. As shown in Fig. 2b, the *J-V* curves of the FPSCs with or without CDs-Cl were measured in reverse scan (RS) and forward scan (FS) under a



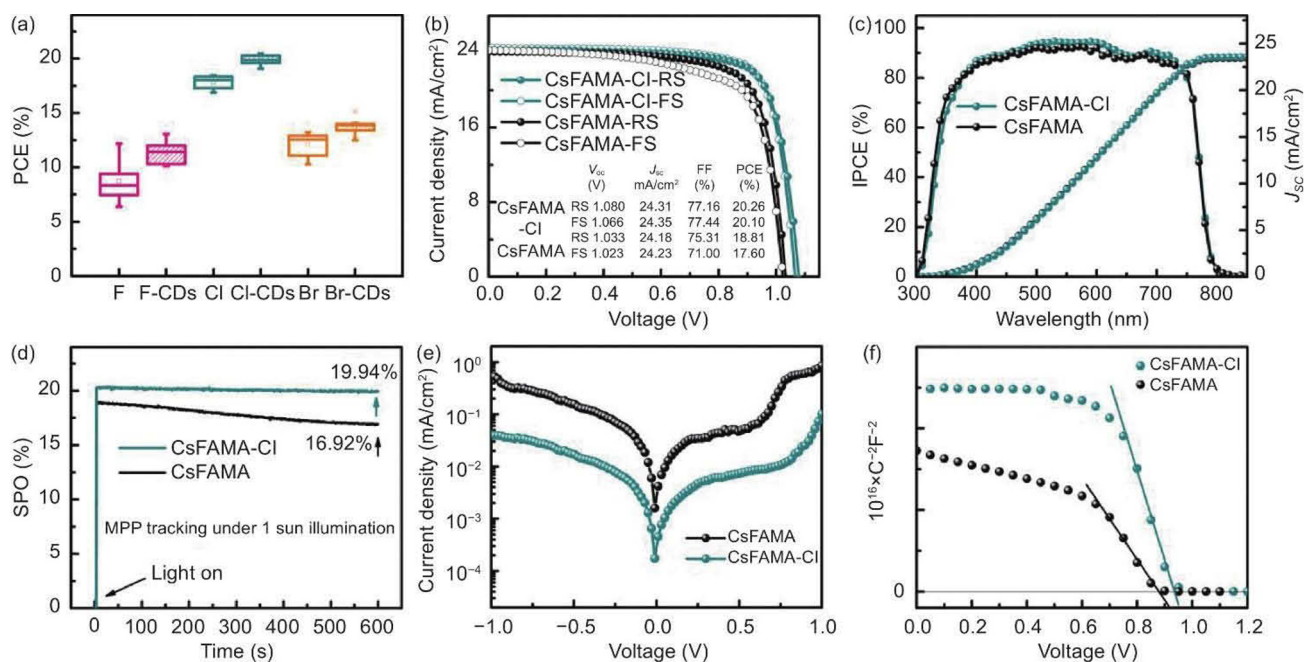


Fig. 2 (a) Statistics of PCEs based on 50 flexible CsFAMA and CsFAMA-T devices. (b)  $J-V$  curves measured by reverse and forward scans of the flexible champion devices of CsFAMA and CsFAMA-Cl. (c) EQE and integrated current density curves for flexible CsFAMA and CsFAMA-Cl devices. (d) Stabilized power outputs of the flexible CsFAMA and CsFAMA-Cl devices. (e) Dark  $J-V$  curves of flexible CsFAMA and CsFAMA-Cl devices. (f) Mott-Schottky plots of CsFAMA and CsFAMA-Cl devices.

simulated sunlight of AM 1.5 G. The reference CsFAMA device achieves a champion PCE of 18.81% in RS, with a short circuit current density ( $J_{sc}$ ) of 24.18 mA cm<sup>-2</sup>, an open circuit voltage ( $V_{oc}$ ) of 1.033 V, and a fill factor (FF) of 75.31%. While the champion device of CsFAMA-Cl yields a PCE of 20.26% with all improved photovoltaic parameters in FS, especially the  $V_{oc}$  (1.080 V) and FF (77.16%). In addition, a negligible hysteresis (0.7%) is presented on the CsFAMA-Cl device in comparison with that of CsFAMA (6.4%). The integrated  $J_{sc}$  values from EQE spectra, which were calculated to be 23.45 and 23.56 mA cm<sup>-2</sup> for CsFAMA and CsFAMA-Cl devices, respectively, match well with the values measured from  $J-V$  curves for all the devices (3% discrepancy, Fig. 1c). Moreover, the CsFAMA-Cl device delivers a stabilized power output (SPO) of 19.94% after operation at the maximum power point under continuous illumination for 600 s, whereas the CsFAMA device exhibits a decreased SPO from initial 18.45% to 16.92% (Fig. 2d).

Fig. 2e shows the dark  $J-V$  curves of flexible devices with or without CDs-Cl, where the current density of the CsFAMA-Cl device is reduced by one order of magnitude relative to the CsFAMA device, which indicates the increased shunt resistance and the suppressed charge carrier recombination and leakage current. By applying the Mott-Schottky ( $M-S$ ) relation<sup>[28]</sup>, the capacitance-voltage ( $C-V$ ) characteristics can reflect interfacial charge density, which is inversely proportional to the straight-line slope of the  $M-S$  plot. The slope of the CsFAMA-Cl device ( $5.4 \times 10^{16}$ ) shown in Fig. 2f is larger than that of CsFAMA ( $2.7 \times 10^{16}$ ) devices, suggesting less charge accumulation at the interface between

perovskite and Spiro-OMeTAD. These two results demonstrate that embedding CDs-Cl into perovskite films can effectively improve the carrier dynamics of their FPSCs.

Long-term experimental and mechanical stability remains as the major challenges restricting the commercialization of FPSCs. We thus evaluated the moisture-stability and thermal stability as well as the mechanical flexibility of the CsFAMA and CsFAMA-Cl devices. As shown in Fig. 3a, the PCE of the CsFAMA device is decreased to 60% after 40 days under the condition of 40% relative humidity at room temperature, whereas the CsFAMA-Cl device still maintains over 90% of its initial efficiency even after 90 days. The thermal stability tracking at 85 °C for the CsFAMA and CsFAMA-Cl devices is shown in Fig. 3b. The CsFAMA device degrades nearly 40% in 200 h, whereas the thermal stability of CsFAMA-Cl device shows an even more significant improvement, where the PCE maintain over 85% of its initial efficiency after annealing of 200 h. The mechanical flexibility of all PSCs was evaluated by bending at different bending curvatures and bending cycles. Fig. 3c shows the bending test with different curvature radii from 8 to 2 mm under 100 bending cycles. The CsFAMA-Cl device still retains 90% of its original efficiency even after bending with 2 mm curvature. In contrast, the CsFAMA device suffers a continuously reduction to 80% when curvature is lowered to 4 mm and a significant degradation with bending further to 2 mm. Furthermore, the bending durability of the CsFAMA and CsFAMA-Cl devices were also plotted as a function of bending cycles under the curvature of 4 mm (Fig. 3d). As expected, the CsFAMA-Cl device is found to maintain over 80% of its initial value after 500 bending

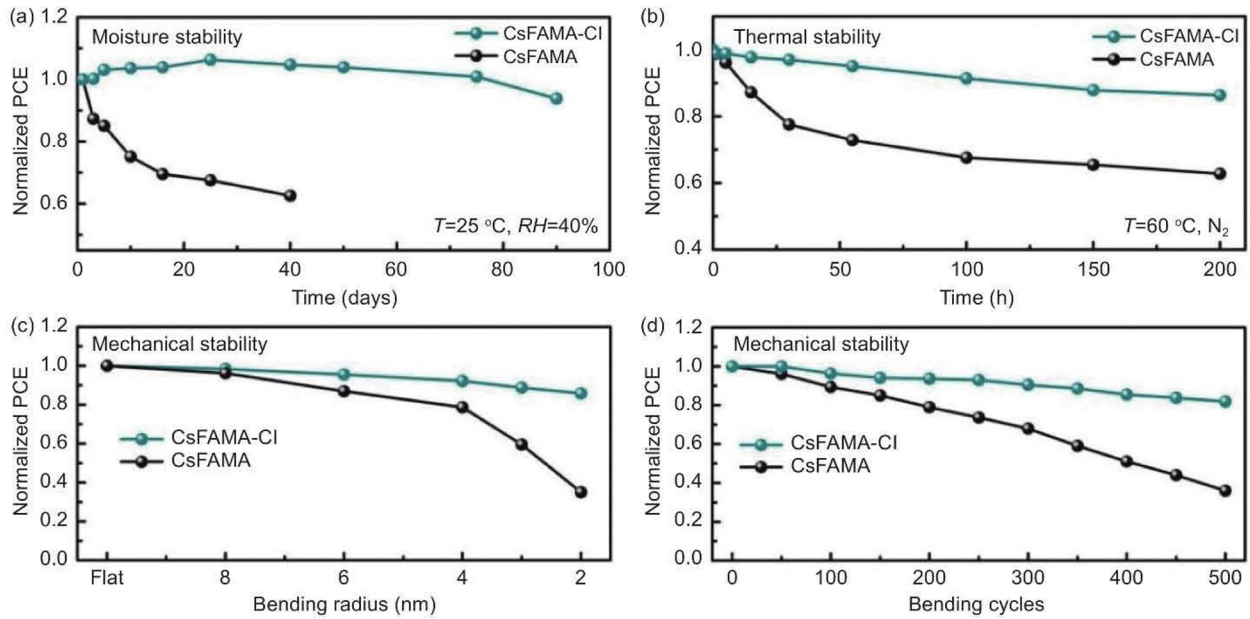


Fig. 3 (a) Moisture stability for flexible CsFAMA and CsFAMA-Cl devices in a relative humidity of 40%. (b) Thermal stability of flexible CsFAMA and CsFAMA-Cl devices under heating stress (85 °C) in an inert atmosphere. (c) PCE evolution of the flexible devices upon increasing bending curvature radius after 100 bending cycles. (d) Bending durability of the flexible devices as a function of bending cycles under the curvature of 4 mm.

cycles. However, the CsFAMA device degrades continuously by more than 60% in 500 cycles. The enhanced environmental and mechanical stability is likely attributed to the embedding of CDs-Cl into perovskite films that inhibits the perovskite from decomposition and ion migration.

To reveal the reason behind the enhanced PCE and the improved stability of the CsFAMA-Cl device, we conducted the characterization on the morphology, structure and optoelectronic properties of corresponding perovskite films. Fig. 4a and b shows the top-view SEM images of the CsFAMA and CsFAMA-Cl films, respectively. It can be observed that the embedding of Cl-CDs leads to no alteration of grain-size but the improvement of the surface smooth and the compactness as compared to the CsFAMA film (see the AFM images in the insets of Fig. 4a and b). This could be attributed to the modulated nucleation and growth kinetics of the perovskite films induced by the introduction of CDs-Cl<sup>[19]</sup>. Also, it can be seen that CDs-Cl is located at surface and GBs in terms of the contrast of electron signals (Fig. 4b). In addition, introduction of CDs-Cl leads to better orientation of perovskite films along the [001] direction perpendicular to the substrate, evidenced by the XRD patterns shown in Fig. 4c. The XRD analysis demonstrates no phase change and no shift of diffraction peaks, which further suggests that CDs-Cl is distributed at surface and GBs of perovskite films<sup>[18]</sup>. Fig. 4d shows UV-vis and PL spectra of the CsFAMA and CsFAMA-Cl films deposited on glass substrates. The PL intensity increases noticeably by the embedding of CDs-Cl, implying the suppressed nonradiative charge recombination. As shown in Fig. 4e, the TRPL decay curves of perovskite films with or without CDs-Cl were fitted by the bi-exponential

functions<sup>[29]</sup>. The CsFAMA-Cl film shows the average carrier lifetime of 145.86 ns, which is about three-fold longer than CsFAMA film (54.25 ns), consistent with the result of steady-state PL.

XPS was further performed to reveal if halogen-terminated CDs could arouse strong chemical interaction with perovskite. Fig. 4f shows the high-resolution XPS spectra of the Pb4f and Cl2p for the CsFAMA and CsFAMA-Cl films. There are two main peaks located at 138.1 and 142.9 eV in the reference CsFAMA film, corresponding to the Pb4f<sub>7/2</sub> and Pb4f<sub>5/2</sub>, respectively. As expected, the peaks from Pb4f shift to higher binding energy (a shift of 0.3 eV) in the CsFAMA-Cl films, indicating the chemical interaction between the CDs-Cl and the Pb in perovskite lattice<sup>[30]</sup>. Furthermore, the Cl2p<sub>3/2</sub> and 2p<sub>1/2</sub> peaks of CDs-Cl exhibit a negative shift of 0.38 eV to 198.78 and 200.39 eV, respectively, further indicating the presence of Pb-Cl interactions between perovskite and CDs-Cl. Such strong interaction is helpful to stabilize the Pb-I octahedral lattice of perovskite. The defect density of the CsFAMA and CsFAMA-Cl films was determined based on the space-charge-limited-current (SCLC) method<sup>[3]</sup>. Fig. 4g and h show the dark *I-V* characteristics of the electron-only (ITO/SnO<sub>2</sub>/CsFAMA/PCBM/Au) and hole-only (ITO/PEDOT:PSS/CsFAMA/Spiro-OMeTAD/Au) devices. The defect density (*N<sub>t</sub>*) can be calculated from the following relation<sup>[3]</sup>:

$$N_t = \frac{2\epsilon\epsilon_0 V_{TFL}}{qL^2}$$

where  $\epsilon$ ,  $\epsilon_0$ ,  $V_{TFL}$ ,  $q$  and  $L$  are the relative dielectric constant, the vacuum permittivity, the onset voltage of the trap-filled

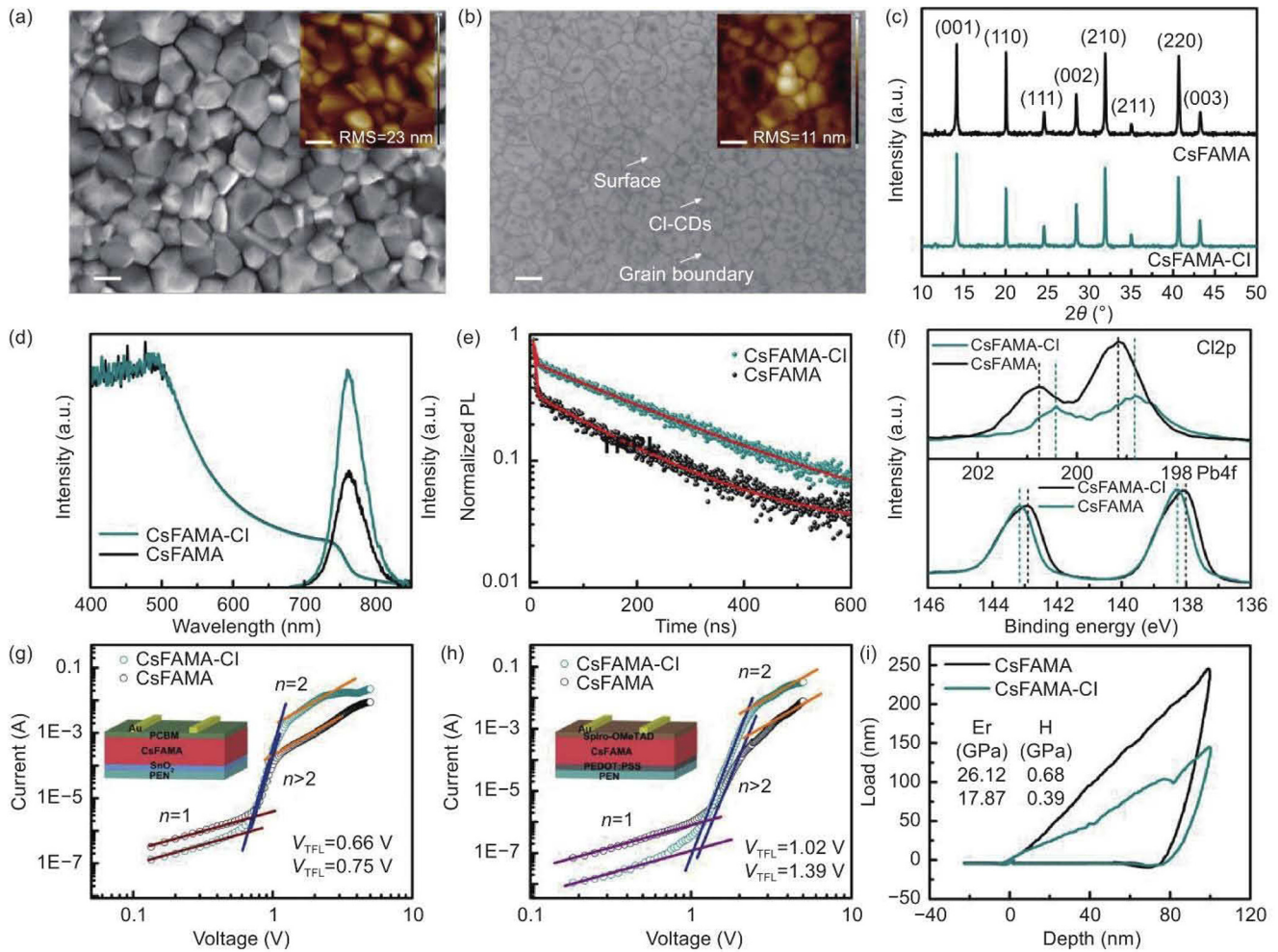


Fig. 4 SEM and AFM images for (a) CsFAMA and (b) CsFAMA-Cl films. The scale bar is 500 nm. (c) XRD patterns of CsFAMA and CsFAMA-Cl films. (d) UV-vis absorption spectra and steady-state PL spectra for the CsFAMA and CsFAMA-Cl films. (e) TRPL spectra for the CsFAMA and CsFAMA-Cl films. (f) Binding energy of Pb4f and Cl2p in XPS spectra for different films. Dark  $I$ - $V$  curves of (g) the electron-only and (h) hole-only devices based on different perovskite films. The insets in (g) and (h) show corresponding device architectures. (i) Loading and unloading force curves for different perovskite films.

limit region, elemental charge, and thickness of the film, respectively.  $N_t$  is linearly proportional to the trap-filled limiting voltage ( $V_{TFL}$ , the kink point between  $n=1$  and  $n>2$  regions) and calculated to be  $1.1 \times 10^{16} \text{ cm}^{-3}$  ( $2.0 \times 10^{16} \text{ cm}^{-3}$ ) and  $9.5 \times 10^{15} \text{ cm}^{-3}$  ( $1.4 \times 10^{16} \text{ cm}^{-3}$ )  $\text{cm}^{-3}$  for the CsFAMA and CsFAMA-Cl films, respectively. Such strong chemical bonding gives rise to the passivation of ionic defects and stabilization of perovskite films, contributing consequently to the highly efficient and stable FPSCs. Embedding the CDs-Cl at surface and GBs also leads to the change of the mechanical performance of perovskite films. As shown in Fig. 4i, the hardness and Young modulus of CsFAMA films decrease from 0.68 to 0.39 GPa and from 26.12 to 17.87 GPa, respectively, presenting a softer behavior. This could be attributed to the crosslinking effects of CDs-Cl between the adjacent grains of polycrystalline perovskite film, which in return enhances the flexibility of perovskite films.

It should be noted that CDs-Cl also play a key role in the modulation of carrier dynamics of perovskite films. We investigated the electronic structures of the perovskite films

via UPS (Fig. 5a). From the secondary electron cutoff spectrum, we observed a change in work function from 4.39 to 4.28 eV between the CsFAMA and the CsFAMA-Cl films. The corresponding energy levels in conduction band were calculated to be 4.22 and 4.11 eV, respectively. From these measurements, we built energy-level diagrams for the two devices (Fig. 5b). The more matched energy level alignment in heterointerfaces of CsFAMA-Cl device enables the decrease of the interfacial charge transport barrier, consequently leading to the boosted  $V_{OC}$  and FF of the flexible PSCs. Regarding the barrier at GBs, as shown in Fig. 5c, we determined the energy level of CDs-Cl by the electrochemical CV method based on the previous reports<sup>[21,22]</sup>. The LUMO and HOMO energy levels of CDs-Cl are calculated to be -4.04 and -5.68 eV, respectively, which are very close to those of bulk perovskite (-4.22 and -5.80 eV, Fig. 5d). Such energy level alignment is thus beneficial to charge extraction and transfer between the adjacent grains of perovskite films. Whereas the insulating GBs within the CsFAMA film provides no charge-selection function and only allows carrier



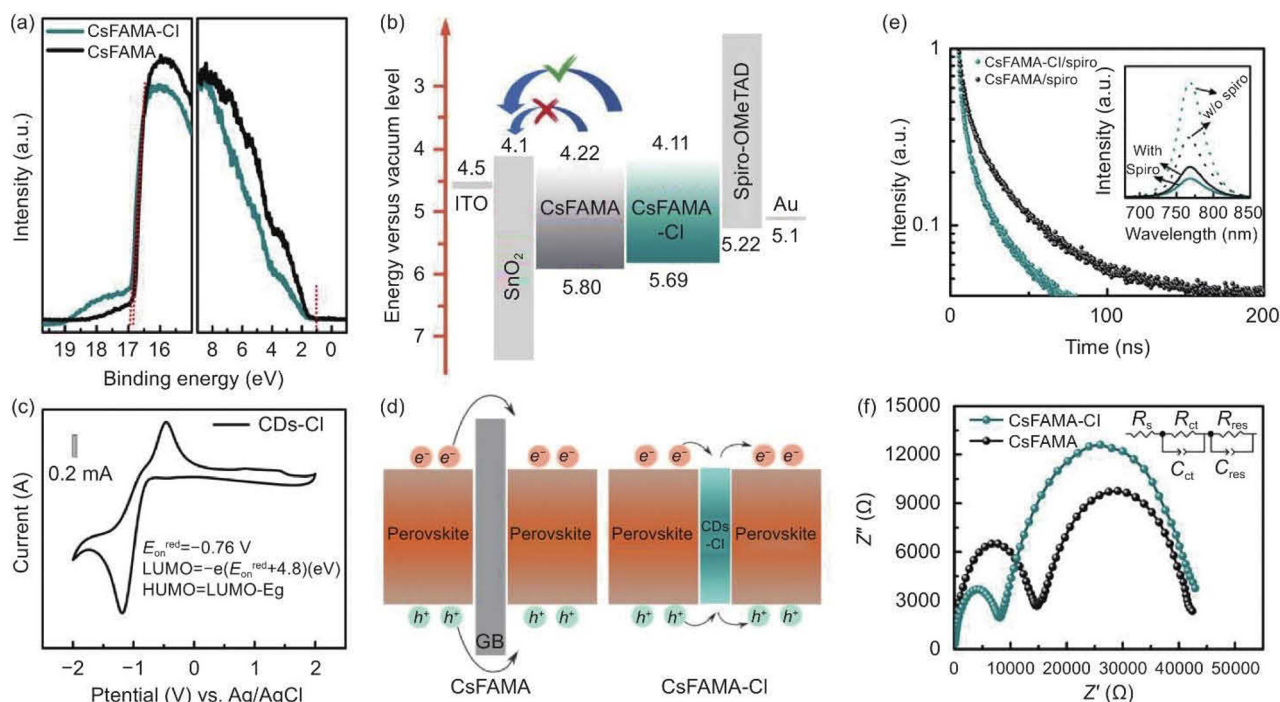


Fig. 5 (a) Helium La (21.22 eV) spectra of secondary electron cutoff (left) and valence band (right). (b) Schematic diagram of energy band for PSCs based on different perovskite films. (c) Cyclic voltammetry scans for CDs-Cl colloidal solution. (d) Schematic energy level diagrams at GBs for CsFAMA and CsFAMA-Cl films. (e) TRPL and steady-state PL (inset) spectra of the CsFAMA and CsFAMA-Cl films with Spiro-OMeTAD layer. (f) EIS of perovskite devices based on the CsFAMA and CsFAMA-Cl films.

tunneling for transport, which is responsible for charge accumulation and  $V_{OC}$  drop.

To experimentally confirm this, the steady-state PL and TRPL for samples in a stack of perovskite/with or without CDs-Cl/Spiro-OMeTAD (Fig. 5e) were measured. The PL intensity of all samples after depositing Spiro-OMeTAD was quenched, demonstrating the hole extraction and collection at perovskite/Spiro-OMeTAD interface. Compared to the control sample, the shortened PL decay after embedding CDs-Cl indicates a faster hole-transfer process and more efficient hole extraction due to the decreased interface barrier (Fig. 5a,b). In addition, electrical impedance spectroscopy (EIS) was further conducted by using an electrochemical workstation with the frequency range from 1 Hz to 1 MHz under 0.8 V in the dark. EIS provides insight into the charge transport process and contact resistance information. The recombination resistance ( $R_{rec}$ ) and the contact resistance ( $R_{ct}$ ) at the perovskite/hole transport layer interface of the PSCs were evaluated. The Nyquist plots shown in Fig. 5f exhibit two diacritical characteristic arcs with high-frequency and low-frequency assigned to the  $R_{ct}$  and the  $R_{rec}$  of charge carriers, respectively. The values of  $R_{ct}$  and  $R_{rec}$  change greatly when the CDs-Cl are introduced. The decreased  $R_{ct}$  suggests that the hole extraction at the perovskite/Spiro-OMeTAD becomes more efficient compared with the control device, consistent with faster charge extraction observed from TRPL results. The increased  $R_{rec}$  reveals CDs-Cl passivation at GBs indeed decreases recombination of charge carriers in perovskite layer. These observations further indicate a synergistic effect on defect

passivation and carrier transport for the CDs-Cl decorated PSCs.

## 4 Conclusions

In summary, present work is demonstration of grafting CDs with a series of halogen terminations that can directly be generated in halobenzene antisolvents, as well as the adopting of such semiconducting nanoparticles as efficient interfacial mediators to address the environmental and mechanical instability of FPSCs. Such interfacial embedding results in strong chemical crosslinking as well as effective defect passivation and carrier dynamics modulation of perovskite films, which leads to the pronounced improvement of the champion PCE of FPSCs up to 20.26%. Without any encapsulation, the CDs-Cl embedded devices exhibit remarkable environmental stability, i.e., retaining over 90% of their initial PCE after 90 days under a relative humidity of 40% as well as delivering a thermal stability of 200 h under thermal stress of 85 °C. Most importantly, strong chemical interaction between CDs-Cl and perovskite enhances the flexibility of perovskite films, contributing consequently to superior robustness of FPSCs against mechanical deformation. This work could thus be inspiring for developing high performance FPSCs through interfacial embedding of carbon-based nanoobjects with rationally tailored surfaces.

## Acknowledgements

This work was financially supported by the project of the



National Key R&D Program for International Cooperation (2021YFE0115100), National Natural Science Foundation of China (52172101, 51972272 and 51872240), Project supported by the Research Fund of State Key Laboratory of Solidification Processing (NPU), China (2022-BJ-05), Shaanxi Province Key Research and Development Program (2022KWZ-04 and 2021ZDLGY14-08), the Fundamental Research Funds for the Central Universities (G2022KY0604). The authors would like to thank the Analytical & Testing Center of Northwestern Polytechnical University and Shaanxi Materials Analysis and Research Center for XPS, XRD, SEM and TEM characterizations.

## References

- [1] Eperon G E, Hörantner M T, Snaith H J. Metal halide perovskite tandem and multiple-junction photovoltaics [J]. *Nature Reviews Chemistry*, 2017, 1(12): 0095.
- [2] Green M A, Ho-Baillie A, Snaith H J. The emergence of perovskite solar cells [J]. *Nature Photonics*, 2014, 8(7): 506-514.
- [3] Dong Q F, Fang Y, Shao Y, et al. Electron-hole diffusion lengths > 175  $\mu\text{m}$  in solution-grown  $\text{CH}_3\text{NH}_3\text{PbI}_3$  single crystals [J]. *Science*, 2015, 347(6225): 967-970.
- [4] Best research-cell efficiency chart (NREL, 2022) [Z]. <https://www.nrel.gov/pv/cell-efficiency.html>.
- [5] Yang L, Feng J S, Liu Z K, et al. Record-efficiency flexible perovskite solar cells enabled by multifunctional organic ions interface passivation [J]. *Advanced Materials*, 2022, 34(24): 2201681.
- [6] Yang D, Yang R X, Priya S, et al. Recent advances in flexible perovskite solar cells: fabrication and applications [J]. *Angewandte Chemie International Edition*, 2019, 58(14): 4466-4483.
- [7] Jia C M, Zhao X Y, Lai Y H, et al. Highly flexible, robust, stable and high efficiency perovskite solar cells enabled by van der Waals epitaxy on mica substrate [J]. *Nano Energy*, 2019, 60: 476-484.
- [8] Hu X T, Meng X C, Zhang L, et al. A mechanically robust conducting polymer network electrode for efficient flexible perovskite solar cells [J]. *Joule*, 2019, 3(9): 2205-2218.
- [9] Li M, Yang Y G, Wang Z K, et al. Perovskite grains embraced in a soft fullerene network make highly efficient flexible solar cells with superior mechanical stability [J]. *Advanced Materials*, 2019, 31(25): 1901519.
- [10] Jeong G, Koo D, Seo J, et al. Suppressed interdiffusion and degradation in flexible and transparent metal electrode-based perovskite solar cells with a graphene interlayer [J]. *Nano Letters*, 2020, 20(5): 3718-3727.
- [11] Luo Q, Ma H, Hou Q Z, et al. All-carbon-electrode-based durable flexible perovskite solar cells [J]. *Advanced Functional Materials*, 2018, 28(11): 1706777.
- [12] Li N, Tao S, Chen Y, et al. Cation and anion immobilization through chemical bonding enhancement with fluorides for stable halide perovskite solar cells [J]. *Nature Energy*, 2019, 4(5): 408-415.
- [13] Guo P F, Ye Q, Liu C, et al. Double barriers for moisture degradation: assembly of hydrolysable hydrophobic molecules for stable perovskite solar cells with high open-circuit voltage. *Advanced Functional Materials*, 2020, 30(28): 2002639.
- [14] Guo P F, Ye Q, Yang X K, et al. Surface & grain boundary co-passivation by fluorocarbon based bifunctional molecules for perovskite solar cells with efficiency over 21%. *Journal of Materials Chemistry A*, 2019, 7(6): 2497-2506.
- [15] Zhao W H, Guo P F, Su J, et al. Synchronous passivation of defects with low formation energies via terdentate anchoring enabling high performance perovskite solar cells with efficiency over 24% [J]. *Advanced Functional Materials*, 2022, 32(24): 2200534.
- [16] Xue Q, Zhang H J, Zhu M S, et al. Photoluminescent  $\text{Ti}_3\text{C}_2$  MXene quantum dots for multicolor cellular imaging [J]. *Advanced Materials*, 2017, 29(15): 1604847.
- [17] Xia C L, Zhu S J, Feng T L, et al. Evolution and synthesis of carbon dots: from carbon dots to carbonized polymer dots [J]. *Advanced Science*, 2019, 6(23): 1901316.
- [18] Guo P F, Yang X K, Ye Q, et al. Laser-generated nanocrystals in perovskite: universal embedding of ligand-free and sub-10 nm nanocrystals in solution-processed metal halide perovskite films for effectively modulated optoelectronic performance [J]. *Advanced Energy Materials*, 2019, 9(35): 1901341.
- [19] Guo P F, Zhu H F, Zhao W H, et al. Interfacial embedding of laser-manufactured fluorinated gold clusters enabling stable perovskite solar cells with efficiency over 24% [J]. *Advanced Materials*, 2021, 33(36): 2101590.
- [20] Yu H, Zhao W H, Ren L, et al. Laser-generated supranano liquid metal as efficient electron mediator in hybrid perovskite solar cells [J]. *Advanced Materials*, 2020, 32(34): 2001571.
- [21] Luo Z, Wu F, Zhang T, et al. Designing a perylene diimide/fullerene hybrid as effective electron transporting material in inverted perovskite solar cells with enhanced efficiency and stability [J]. *Angewandte Chemie International Edition*, 2019, 58(25): 8520-8525.
- [22] Ravi V K, Markad G B, Nag A. Band edge energies and excitonic transition probabilities of colloidal  $\text{CsPbX}_3$  ( $\text{X} = \text{Cl}$ ,

- Br, I) perovskite nanocrystals [J]. *ACS Energy Letters*, 2016, 1(4): 665-671.
- [23] Zhao J, Tang L, Xiang J, et al. Chlorine doped graphene quantum dots: Preparation, properties, and photovoltaic detectors [J]. *Applied Physics Letters*, 2014, 105(11): 111116.
- [24] Zhang X R, Yang J Y, Ren Z Y, et al. In situ observation of electrolyte-dependent interfacial evolution of graphite anode in sodium-ion batteries via atomic force microscopy [J]. *New Carbon Materials*, 2022, 37(2): 371-380.
- [25] Xu F, Zhai Y X, Zhang E, et al. Ultrastable surface-dominated pseudocapacitive potassium storage enabled by edge-enriched N-doped porous carbon nanosheets [J]. *Angewandte Chemie International Edition*, 2020, 59(44): 19460-19467.
- [26] Wang Z Q, Xuan J N, Zhao Z G. et al. Versatile cutting method for producing fluorescent ultrasmall MXene sheets [J]. *ACS Nano* 2017, 11(11): 11559-11565.
- [27] Bu T, Wu L, Liu X, et al. Synergic interface optimization with green solvent engineering in mixed perovskite solar cells [J]. *Advanced Energy Materials*, 2017, 7(20): 1700576.
- [28] Bu T, Li J, Zheng F, et al. Universal passivation strategy to slot-die printed SnO<sub>2</sub> for hysteresis-free efficient flexible perovskite solar module [J]. *Nature Communications*, 2018, 9: 4609.
- [29] Cho H, Jeong S H, Park M H, et al. Overcoming the electroluminescence efficiency limitations of perovskite light-emitting diodes [J]. *Science*, 2015, 350(6265): 1222-1225.
- [30] Wang R, Xue J, Wang K L, et al. Constructive molecular configurations for surface-defect passivation of perovskite photovoltaics [J]. *Science*, 2019, 366(6472): 1509-1513.